JACS
JOURNAL OF THE AMERICAN CHEMICAL SOCIETY
pubs.acs.org/JACS
Article

Quantitative Agreement between Conformational Substates of Holo Calcium-Loaded Calmodulin Detected by Double Electron−Electron Resonance EPR and Predicted by Molecular Dynamics Simulations

Thomas Schmidt, David Wang, Jaekyun Jeon, Charles D. Schwieters, and G. Marius Clore*

Cite This: J. Am. Chem. Soc. 2022, 144, 12043−12051
Read Online

ABSTRACT: Calcium-loaded calmodulin ($CaM/4Ca^{2+}$) comprises two domains that undergo rigid body reorientation from a predominantly extended conformation to a compact one upon binding target peptides. A recent replica-exchange molecular dynamics (MD) simulation on holo $CaM/4Ca^{2+}$ suggested the existence of distinct structural clusters (substates) along the path from extended to compact conformers in the absence of substrates. Here, we experimentally demonstrate the existence of $CaM/4Ca^{2+}$ substates trapped in local minima by three freezing/annealing regimes (slow, 40 s; intermediate, 1.5 s; fast, 0.5 ms) using pulsed Q-band double electron−electron resonance (DEER) EPR spectroscopy to measure interdomain distances between nitroxide spin-labels positioned at A17C and A128C in the N- and C-terminal domains, respectively. The DEER echo curves were directly fit to population-optimized $P(r)$ pairwise distance distributions calculated from the coordinates of the MD clusters and compact crystal structure. DEER data on fully deuterated $CaM/4Ca^{2+}$ were acquired at multiple values of the second echo period (10−35 μs) and analyzed globally to eliminate instrumental and overfitting artifacts and ensure accurate populations, peak positions, and widths. The DEER data for all three freezing regimes are quantitatively accounted for within experimental error by 5−6 distinct conformers comprising a predominantly populated extended form (60−75%) and progressively more compact states whose populations decrease as the degree of compactness increases. The shortest interdomain separation is found in the compact crystal structure, which has an occupancy of 4−6%. Thus, $CaM/4Ca^{2+}$ samples high energy local minima comprising a few discrete substates of increasing compactness in a rugged energy landscape.

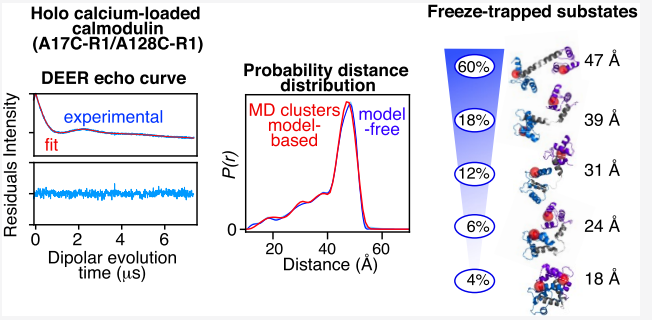

INTRODUCTION

Conformational substates of proteins play a key role in protein folding and molecular recognition.[1,2] In the context of large interdomain rearrangements associated with ligand binding, the free energy landscape[3,4] describing the transition from the apo form to the bound form, just as in protein folding,[5−7] is likely to be rugged with numerous local minima along the pathway. Moreover, even in the absence of ligands, many highly transient conformational substates comprising sparsely populated local minima may be sampled, some of which are likely to be close but not identical to the ligand-bound conformation.[8,9] A key question lies in determining exactly what conformations are sampled by protein substates. Conformational substates were first inferred on kinetics grounds in studies on carbon monoxide rebinding to myoglobin over a wide range of temperatures spanning from liquid helium temperatures to room temperature.[2,3,10] To date, however, most of the structural information on substates has been gleaned from molecular dynamics (MD) modeling studies.[1] Here, we show, using the universal eukaryotic calcium sensor calmodulin (CaM)[11] as an example, that, in suitable cases, substates can be detected experimentally by double electron−electron resonance (DEER) EPR spectroscopy and that population-optimized clusters obtained from molecular dynamics simulations can quantitatively account for the DEER data within experimental error.

CaM provides a classical example of a protein undergoing large interdomain rearrangement upon substrate binding that is critical to its function as the major calcium sensor within all eukaryotic cells.[12−18] CaM comprises N- and C-terminal calcium-binding domains connected by a linker. In all but one crystal structure,[19] holo calcium-loaded CaM ($CaM/4Ca^{2+}$) (i.e., in the absence of a bound protein/peptide substrate) adopts an extended dumbbell conformation in which the linker forms a continuous rigid helix, known as the "central" helix.[11]

Received: February 25, 2022
Published: June 27, 2022

https://doi.org/10.1021/jacs.2c02201
J. Am. Chem. Soc. 2022, 144, 12043−12051

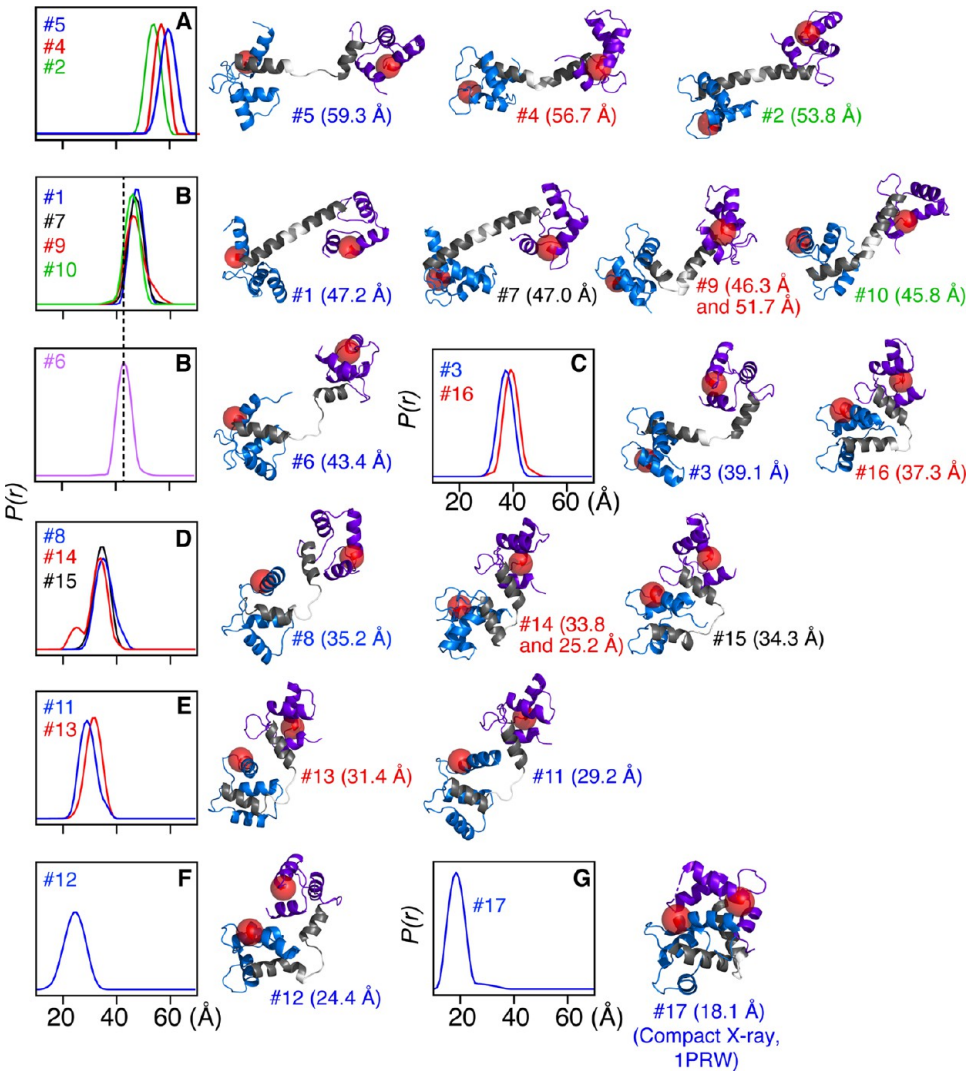

Figure 1. Ribbon diagrams of representative structures from the 16 clusters obtained from a 460 ns replica-exchange solute-tempering MD simulation[33,34] on holo CaM/4Ca^{2+} and of the compact crystal structure (1PRW)[19] of holo CaM/4Ca^{2+} together with the corresponding $P(r)$ distributions between A17C-R1 and A128C-R1 calculated from a R1 rotamer library.[18] The MD clusters can be grouped into six families (A−F), with the compact crystal structure as a seventh family (G). The positions of the R1 nitroxide labels are indicated by red spheres located at the relevant backbone Cα atoms for visualization purposes only. The N- and C-terminal domains of CaM/4Ca^{2+} are colored in blue and purple, respectively, with the linker region shown in gray. The distance corresponding to the peak of the $P(r)$ distribution is indicated below each model. The $P(r)$ distributions are calculated from a weighted ensemble of nitroxide oxygen positions based on molecular coordinates of the structures, as described previously.[18] Because the nitroxide labels are represented as a weighted ensemble, the shape of the calculated $P(r)$ distribution can be non-Gaussian and can include shoulders or separate peaks that correspond to distinct regions of conformational space occupied by one or both nitroxide labels.

In solution, however, NMR has clearly shown that the middle four residues of the "central" helix are not rigid but dynamic and partially disordered.[20] Thus, although the overall shape of holo CaM/4Ca^{2+} in solution is predominantly extended, the two domains reorient relative to one another and, for the majority of the time, sample a cone of semi-angle ∼30−40°, as assessed by extended Lipari−Szabo analysis[21] of heteronuclear relaxation data,[22] as well as maximum occurrence analysis of residual dipolar coupling, paramagnetic pseudo-contact shift, small-angle X-ray scattering, and EPR data.[23−28] Sparsely populated (<5%) compact states of holo CaM/4Ca^{2+} are also sampled in the absence of substrates, as evidenced by interdomain paramagnetic relaxation enhancement studies.[9,29] These compact states occupy a relatively broad region of conformational space that encompasses the compact holo CaM/4Ca^{2+} crystal structure (PDB code 1PRW)[19] and is close to but not identical to that found in a wide array of CaM/4Ca^{2+}−substrate complexes[9] where the two domains of CaM clamp peptide substrates in a manner similar to two overlapping hands holding a rope.[30] Single-molecule Förster resonance energy transfer[31] and cross-section measurements by mass spectrometry−ion-mobility spectrometry in a solvent-free environment[32] also provide evidence for the existence of a compact state of holo CaM/4Ca^{2+} coexisting with the dumbbell extended conformation but do not reveal the presence of distinct substates.

RESULTS AND DISCUSSION

MD-Derived Structure Clusters and Calculated *P*(*r*) Distributions. Recently, a new method of inflection core state

https://doi.org/10.1021/jacs.2c02201
J. Am. Chem. Soc. 2022, 144, 12043−12051

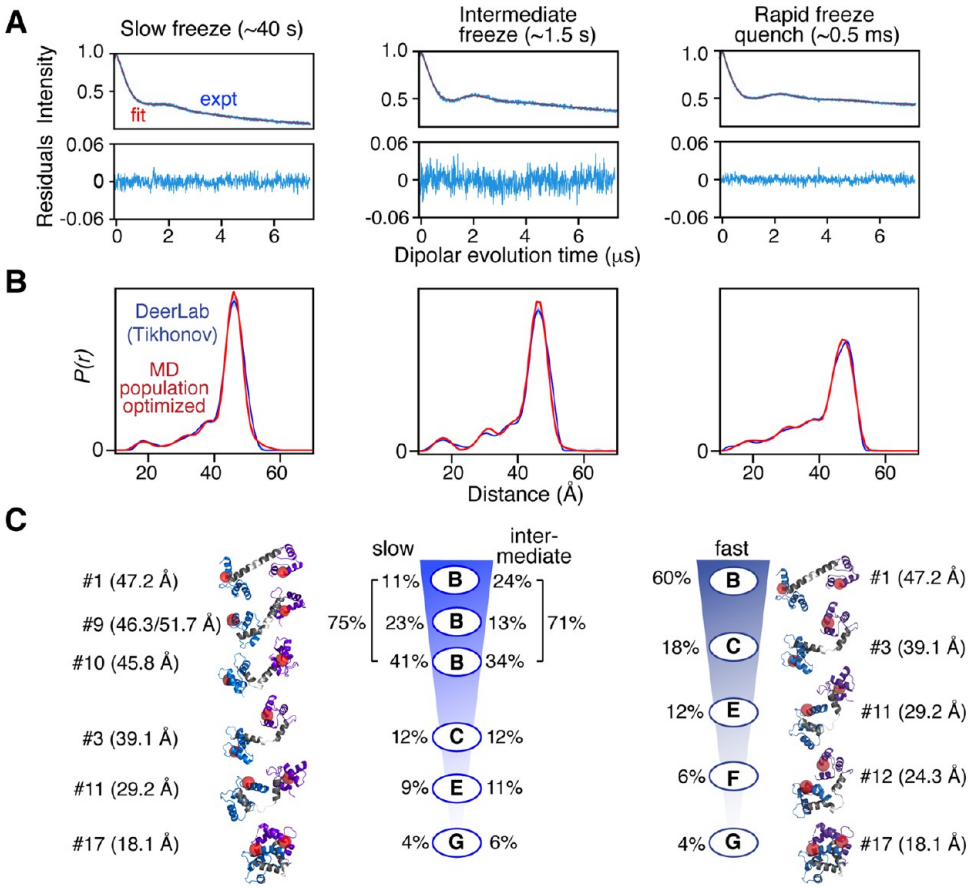

Figure 2. CaM/4Ca^{2+} substates. (A) Examples of raw DEER echo curves (blue) recorded at a second echo period time T = 20 μs for slow frozen (left), intermediate rate frozen (middle), and rapidly frozen freeze-quenched (right) samples. The red curves are the best fits obtained by population optimization of the $P(r)$ distributions for models 1−17 shown in Figure 1 using the GlaDDvu[47,48] fitting routines imported into a Python script.[18] The time traces of residuals between observed and calculated DEER echo curves are shown below. The complete set of DEER echo curves and corresponding residuals for all values of T are provided in Figures S2A−S4A. (B) Comparison of the $P(r)$ distributions obtained by globally fitting the DEER echo curves at all values of T using either model-free validated Tikhonov regularization in the program DeerLab[46] (blue with light blue representing upper and lower error estimates) or the population-optimized $P(r)$ distributions for models 1−17 shown in Figure 1 (red). The integral under the $P(r)$ distributions has been normalized to 1. (C) Optimized populations of the substates contributing to the DEER echo curves. For the slow and intermediate freezing regimes, the total populations of family B, represented by the sum of the populations of clusters #1, #9, and #10 are shown. For the fast freezing regime, only cluster #1 is present from the B family. (Note that cluster #7 is also present in family A, but the $P(r)$ distribution for cluster #7 is virtually identical to that for cluster #1, and therefore clusters #1 and #7 cannot be distinguished. Consequently, only cluster #1 was included in the calculations). The populations systematically decrease as the interdomain separation decreases and the degree of compactness increases. Further, the population of the extended states (interspin distance $r \sim 46$−47 Å) relative to that of the compact ones ($r \leq 39$ Å) decreases with increasing freezing rate.

clustering, based on Gaussian mixtures, was used to extract 16 well-defined core substates (clusters)[33] from the free energy landscape of a 460 ns replica-exchange solute-tempering MD simulation on holo CaM/4Ca^{2+}.[34] These substates, which range from extended to compact, provide a pathway between extended and compact forms and suggest that the transition between substates is driven by electrostatic interactions; while the trajectory used a TIP3P water model, bias toward compact structures was counteracted through the use of a wide range of temperatures (spanning 300−545 K) in the replica-exchange solute-tempering procedure.[33] Ribbon diagrams of a representative structure from each cluster (models 1−16) together with the crystal structure (PDB code 1PRW) of the compact form of holo CaM/4Ca^{2+} (model 17)[19] are displayed in Figure 1. DEER yields probability distance distributions, $P(r)$, between pairs of spin labels,[35] and the two sites of R1 nitroxide spin-labeling[36,37] at A17C and A128C in the N- and C-terminal domains, respectively, are indicated on the ribbon diagrams by the red spheres. The expected $P(r)$ distributions calculated from the molecular coordinates,[18] based on a rotamer library of the R1 nitroxide side chain implemented in Xplor-NIH,[38] are shown alongside the structures. Model 1 is closest to the extended dumbbell X-ray structure of holo CaM/4Ca^{2+} (backbone rmsd of ~3 Å) with a $P(r)$ peak at 47 Å; the $P(r)$ peaks for the remaining MD structures range from 59 Å (model 5) to 24 Å (model 16); and finally, the $P(r)$ peak for the compact X-ray structure (model 17) of holo CaM/4Ca^{2+} is at 18 Å. From the perspective of the distance between the A17C-R1 and A128C-R1 nitroxide spin-labels, the replica exchange MD clusters can be grouped into five families (A, ~54 to 59 Å; B, ~43 to 47 Å; C, ~37 to 39 Å; D, ~34 to 35 Å; E, 29 to 31 Å; and F, ~24 Å). It is worth noting that the distance of ~18 Å between the two spin-labels in the compact holo crystal structure[19] (model 17, family G) is smaller (i.e., a higher degree of compactness) than that observed with the M13 peptide substrate-bound, either in the compact binding

https://doi.org/10.1021/jacs.2c02201
J. Am. Chem. Soc. 2022, 144, 12043−12051

intermediate (interspin distance ~ 21 Å) or the final complex (interspin distances ~21 and 26 Å arising from two distinct regions of conformational space occupied by the R1 label at A128C).[18]

DEER Data Acquisition. The experimental DEER data were acquired at Q-band and 50 K on CaM/4Ca^{2+}(A17C-R1/A128C-R1). These two labeling sites do not affect the structure of CaM/4Ca^{2+} and only result in a very small reduction (less than a factor of 2) in the affinity for peptide substrates.[9] CaM/4Ca^{2+}, the glycerol cryoprotectant (30% v/v) and the solvent were fully deuterated to increase the phase memory relaxation time (T_m, the timescale for transverse relaxation of a nitroxide spin-label by flip-flop transitions of neighboring protons) by removing electron−proton dipolar interactions.[39−41] This not only increases the signal-to-noise ratio but also ensures that the $P(r)$ distribution derived from the DEER data is not impacted by differential T_m relaxation and therefore accurately reflects the populations of substates present in the sample.[18,40,42] Since the trapping of substates can be influenced by the freezing rate (i.e., the annealing regime), three freezing/annealing conditions were employed: slow (~ 40 s) freezing by placing the 1 mm (internal diameter) quartz EPR tube in a −80 °C freezer;[43] intermediate rate (1.5 s) freezing by directly placing the EPR tube in liquid nitrogen (77 K);[43] and rapid (~0.5 ms) freezing by spraying the sample in the form of a high-speed jet onto a spinning copper disk cooled to 77 K.[18,44,45] For each freezing condition, six sets of DEER echo curves were acquired, with the second echo period time ($T = 2\tau_2$) set to 10, 15, 20, 25, 30 and 35 μs (Figure S1), and the data at all values of T were analyzed globally.[18] The accuracy of peak positions and widths is dictated by the maximum length of the dipolar evolution time, t_{max}, which was set to 7.5 μs except for the data at T = 10 and 15 μs, where t_{max} was set to 4 and 6 μs, respectively. At t_{max} = 7.5 μs, accurate distances and widths are obtained up to $50(t_{max}/2)^{1/3} \sim 78$ Å and $40(t_{max}/2)^{1/3} \sim 62$ Å, respectively.[35]

Analysis of DEER Echo Curves. The DEER data were analyzed in three different ways. First, the DEER echo curves were fitted individually using validated Tikhonov regularization implemented in the program DeerLab.[46] This procedure, which is model-independent, provides a baseline for how well the data can be fitted, given that the constraints imposed by fitting the data at all T values simultaneously will generally result in an increase in the reduced χ^2. It is also important to note that fitting each DEER echo curve individually may result in overfitting the data such that extraneous peaks may appear in the $P(r)$ distributions, which are not reproduced at the different values of T. Second, the DEER echo curves at all values of T were fitted globally by validated Tikhonov regularization in DeerLab.[46] This procedure which ensures that only a single set of peaks in the $P(r)$ distribution represents the DEER data at all values of T, eliminates both instrumental and overfitting artifacts and ensures accurate peak positions and linewidths. Lastly, the DEER data were analyzed globally using GLADDvu[47,48] to directly fit the calculated $P(r)$ distributions for the 17 structure models shown in Figure 1 to the DEER echo curves while optimizing the population of each model. A two-step procedure was employed. In the first pass, the populations of all 17 models were optimized; in the second pass, all models whose populations optimized toward zero were eliminated, and the optimization process was repeated with the remaining models. An example of the fits to the population-optimized, structure-based $P(r)$ distributions for the T = 20 μs DEER data is shown in Figure 2A; the complete set of DEER data together with fits and corresponding residuals is provided in Figures S2A−S4A. A summary of the reduced χ^2 values of the fits to the experimental DEER data is given in Table 1. Within the specified uncertainties, the average reduced χ^2 for the individual fits by Tikhonov regularization are similar to those obtained from the global fits, and the reduced χ^2 values for the global fits obtained by Tikhonov regularization and population optimization of the 17 model $P(r)$ distributions are also comparable (Table 1); the same is true for the time traces of residuals for all three fits (Figures S2A−S4A). In contrast, the $P(r)$ distribution calculated for the cluster populations derived from the replica-exchange solute-tempering MD simulation[33] (Table S1) fail to reproduce the experimental DEER data (Table 1 and Figure S5).

Table 1. Reduced χ^2 of the Fits to the Experimental DEER Echo Curves

freezing regime	DeerLab individual fits[a,b]	DeerLab global fits[a,c]	global population-optimized substates fits[c,d]	global fit to MD cluster populations[c,e]
slow (~40 s)	1.07 ± 0.12	1.14	1.17	3.59
intermediate (~1.5 s)	0.99 ± 0.10	1.06	1.16	4.67
fast (~0.5 ms)	1.01 ± 0.08	1.07	1.00	7.23

[a]Validated Tikhonov regularization. [b]The DEER echo curves at each value of T are fitted individually. The standard deviation represents the variation in χ^2 values obtained for the data recorded at the six values (10 to 35 μs) of T. [c]The DEER echo curves at all values of T ranging from 10 to 35 μs are fitted simultaneously. [d]Fits to the DEER echo curves are based on population-optimized $P(r)$ distributions calculated from the molecular coordinates of the MD clusters (models 1−16) and the compact holo X-ray structure[19] (model 17) using the fitting routines from the program GLADDvu imported into an in-house Python script that also incorporates population optimization. [e]Fits of the $P(r)$ distributions calculated from the molecular coordinates of the MD clusters (models 1−16) using the cluster populations from the replica-exchange solute-tempering MD simulation.[33] The global fits were carried out using the program GLADDvu imported into an in-house Python script.

Quantitative Analysis of Substates and Their Populations. For each freezing regime, the $P(r)$ distributions obtained for CaM/4Ca^{2+} (A17C-R1/A128C-R1) by global direct fitting of the DEER echo curves at multiple values of T using model-free (Tikhonov regularization, blue curves) and model-dependent (population optimization of precalculated distance distributions from molecular coordinates, red curves) methods are basically superimposable (Figure 2B). Of note, however, is that the $P(r)$ distributions obtained from the individual Tikhonov regularization fits (Figures S2B−S4B), while displaying the same overall features, clearly display significant variation for the different T values, including differences in number and intensity of the smaller $P(r)$ peaks, likely due to a combination of instrumental artifacts and overfitting that is circumvented by the global fitting process, whether model-free or model-dependent, at multiple values of T simultaneously. In each instance, four $P(r)$ peaks are observed: a major peak at 46−48 Å corresponding to the predominant extended dumbbell conformation and smaller intensity peaks at 38, 30−32, and 17−18 Å, reflecting increasingly compact conformations (Table 2). The shortest

https://doi.org/10.1021/jacs.2c02201
J. Am. Chem. Soc. 2022, 144, 12043−12051

Table 2. Peak Positions in the $P(r)$ Distributions Obtained from Global Fitting of the DEER Data by Model-Free Tikhonov Regularization

freezing regime	distance (Å)
slow (~40 s)	46, 38, 32, 18
intermediate (~1.5 s)	46, 38, 30, 17
fast (~0.5 ms)	48, 38, 30, 18

distance peak corresponds to the compact holo CaM/4Ca^{2+} crystal structure and is not represented by the MD clusters (Figure 1). There is no evidence in the DEER-derived $P(r)$ distributions obtained by Tikhonov regularization for the presence of any conformers with an interspin separation ≥54 Å (i.e., models 2, 4, and 5; see Figure 1).

The optimized populations of the structures used to reproduce the DEER echo curves are shown in Figure 2C and Table 3. It is important to note that the species and/or

Table 3. Species Populations from Population-Optimized Direct Fitting to DEER Echo Curves

structure model[a] (distance peak in $P(r)$ distribution)	population (%)		
	slow freezing (~40 s)	intermediate freezing (~1.5 s)	fast freezing (0.5 ms)
1 (47.2 Å)	11 ± 2[b]	24 ± 2[b]	60 ± 1
9 (46.5/51.7 Å)	23 ± 2	13 ± 3	
10 (45.8 Å)	41 ± 3	34 ± 2	
3 (39.1 Å)	12 ± 1	12 ± 1	18 ± 1
11 (29.2 Å)	9 ± 1	11 ± 1	12 ± 1
12 (24.4 Å)			6 ± 1
17 (18.1 Å)	4 ± 1	6 ± 1	4 ± 1

[a]Models 1−16 are the MD clusters[33] and model 17 is the compact crystal structure (1PRW)[19] shown in Figure 1. The DEER data obtained for the slow and intermediate rate freezing samples are reproduced by five of the 16 MD clusters together with the compact crystal structure; for the freeze-quenched sample, four of the MD clusters together with the crystal structure reproduce the DEER data. The populations of models not listed in the table optimized to very low values (≪0.1%) in the first pass of calculations and were subsequently excluded from the second pass. Ribbon diagrams of the clusters populated in the global fits are shown in Figure 2C. [b]In the case of the slow and intermediate freezing regime samples, models 1 (r = 47.2 Å) and 7 (r = 46.8 Å) are interchangeable and the choice does not impact the fit to the DEER echo curves.

populations that reproduce the DEER echo curves within experimental error for a given freezing condition do not fit the DEER echo curves for the other two freezing conditions; in other words, the differences in species populations between the three freezing conditions are significant (Table 4 and Figures S6−S8). This is particularly obvious when looking at the time traces of residuals when the fast freezing $P(r)$ populations are used to fit the DEER data for the slow and intermediate rate freezing regimes and vice versa (SI Figures S6−S8).

Only a small subset of the MD clusters,[33] in conjunction with the compact holo CaM/4Ca^{2+} crystal structure,[19] are required to represent the DEER data. The DEER data for the samples obtained with slow and intermediate rate freezing can be fully accounted for by the same set of six models: five from the MD clusters (comprising three elongated structures with a pairwise distance r between spin-labels of ~46−47 Å and two increasingly compact structures with r ~39 and ~29 Å) plus the compact crystal structure (r ~ 18 Å). The extended

Table 4. Reduced χ^2 Values Obtained with the Population-optimized $P(r)$ Distribution for a Given Freezing Regime Versus the Experimental DEER Echo Curves for the Other Two Freezing Regimes

population-optimized $P(r)$ distribution for the specified freezing regime	reduced χ^2 to DEER echo curves		
	slow freezing (~40 s)	intermediate freezing (~1.5 s)	fast freezing (~0.5 ms)
slow (~40 s)	**1.17**[a]	1.31	1.92
intermediate (~1.5 s)	1.32	**1.16**[a]	1.66
fast (~0.5 ms)	2.51	1.87	**1.00**[a]

[a]The values in bold are the reduced χ^2 values for the fits to the experimental DEER echo curves for the specified freezing regime (reported in the third column of Table 1).

structures are the most highly populated, with an overall population of 75 and 71% for the slow and intermediate rate frozen samples, respectively. Interestingly, the partitioning of the extended structures is not identical between the two samples. Further, it is of interest that three extended structures with pairwise interspin distances of ~46−47 Å are required to account for the DEER data; this is because the calculated $P(r)$ distributions for these structures, while very similar, are not identical (Figure 1, second row). The species populations decrease as the degree of structural compactness increases, with the compact holo crystal structure having the lowest occupancy (~4−6%). In the case of the freeze-quenched sample, only one extended conformation, model 1 (the closest to the extended dumbbell crystal structure[12]) is sampled with a population of ~60%; three compact MD clusters with decreasing occupancy as the compactness increases, are sampled, two of which (models 3 and 11) are the same as those from the two other freezing regimes, together with an additional cluster (model 12 populated at ~6%) with r ~ 24 Å; and finally, the compact crystal structure is sampled at a population of ~4%. Interestingly, the compact structure (model 3) with r ~ 39 Å is more highly populated in the freeze-quenched sample (~18%) than in the other two samples (~12%), while that with r ~ 29 Å (model 11) is populated at approximately the same level (9−12%) in all three samples.

To ascertain the robustness of the species populations, we also carried out a series of calculations in which structures within a given family comprising similar $P(r)$ distributions were permuted, leaving out a single structure at a time. The results are summarized in the SI, Tables S2−S6. This procedure yields average populations (SI, Table S2) that are very similar to those shown in Figure 2C and reported in Table 3 and also serves as a control for variations in the $P(r)$ distributions calculated from the molecular coordinates of the replica exchange MD clusters and of the compact crystal structure (1PRD)[19] of holo CaM/4Ca^{2+}.

Comparison with Intermolecular PRE Measurements. In solution, there is rapid interconversion (on the nanosecond timescale) between the substates, and it is therefore of interest to ascertain whether the compact substates identified by DEER in the frozen state can qualitatively reproduce features of the interdomain paramagnetic relaxation enhancement (PRE) profiles observed by solution NMR.[9] Note that only a qualitative comparison with solution PRE data is appropriate since a continuum of conformational states is sampled in solution[22−29] as k_BT (where k_B is the Boltzman constant and T, the temperature) lies above the energy barriers between local

https://doi.org/10.1021/jacs.2c02201
J. Am. Chem. Soc. 2022, 144, 12043−12051

energy minima. The spin-label and spin-labeling sites for the PRE measurements are identical to those used for DEER, except that only one site is labeled at a time. The PRE is exquisitely sensitive to the presence of short-lived, sparsely populated conformations with short distances between the spin-label on one domain and protons on the other, owing to $\langle r^{-6} \rangle$ dependence of the PRE combined with the large magnetic moment of the unpaired electron giving rise to very large values of the transverse PRE rate, Γ_2, at short unpaired electron−proton distances.[50] The computed transverse PRE profiles for the five structures that account for the DEER data obtained with rapid freeze-quenching are compared to the experimental interdomain PRE profiles in Figure 3. While the two domains of CaM/4Ca^{2+} in the two extended structures (models 1 and 3, interspin distances ≥39 Å) do not contribute, as expected, to the interdomain PRE profiles, distinct features of the PRE profiles are qualitatively reproduced by the three compact structures with interspin distances ≤29 Å (namely, models 11 and 12 from the MD clusters, together with the compact crystal structure), thereby providing a link between rapidly interconverting conformations in solution and substates trapped in local minima by freezing and observed by DEER EPR.

Concluding Remarks. In conclusion, three different freezing/annealing regimes trap a small number of holo CaM/4Ca^{2+} substates that can be directly observed by DEER. The substates include both predominantly extended and less populated, progressively more compact structures that are trapped in local minima within a rough free energy landscape. Although the populations of the clusters[33] obtained by analysis of replica-exchange solute-tempering MD simulations[49] do not reproduce the experimental DEER echo curves or the $P(r)$ distributions obtained by Tikhonov regularization (Table 1 and SI Figure S5), the MD clusters sample the "relevant" conformations measured in terms of interdomain distances between two spin-labels positioned at A17C-R1 and A128C-R1. Hence, population optimization of the replica exchange MD clusters in combination with the compact crystal structure of holo CaM/4Ca^{2+} quantitatively reproduces the DEER echo curves within experimental error (Table 1, Figure 2A, and SI Figures S2−S4). Further structural refinement of the relative interdomain orientations in the substates would require the acquisition of DEER data on a series of samples with nitroxide spin-labels positioned at multiple sites within the domains.

Of note is that rapid freeze-quenching results in not only a higher proportion of compact states ($r \leq 39$ Å) relative to the slow and intermediate freezing regimes (~40% versus ~25−30%) but also skews the population of extended states (family B) to the most extended member within that family (such that only model 1 is represented in the B family for the rapid freeze-quenched sample) (Figure 2C and Table 3). The latter is also consistent with the finding that within the B family of clusters, the population of model 1 is increased, while the populations of models 9 and 10 are decreased for the intermediate freezing regime compared to the slow freezing one (Figure 2C and Table 3). These observations can be rationalized as follows. Rapid freeze-quenching provides a glimpse of the room temperature distribution, which is broad and traps substates in the closest higher local energy minima. Slow freezing, on the other hand, allows the system to gently anneal and slowly settle into the low temperature, lower energy, local minima. Hence, the $P(r)$ distributions are narrower for the slow and intermediate freezing regimes than for the rapid freeze-quenched one (Figure 2B and SI Figure S9).

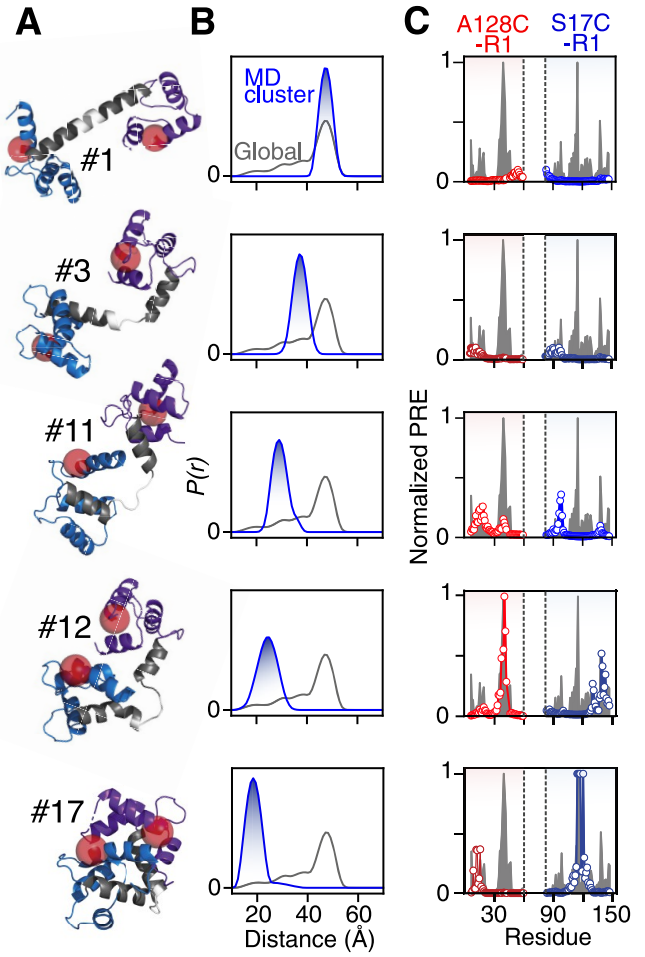

Figure 3. Clusters that reproduce the experimental DEER data for freeze-quenched CaM/4Ca^{2+} reproduce features of the experimental interdomain paramagnetic relaxation enhancement (PRE) profiles obtained by solution NMR.[9] (A) Ribbon diagrams of the clusters with the N- and C-terminal domains in blue and purple, respectively, and residues comprising the "central helix" in the dumbbell crystal structure[12] of holo CaM/4Ca^{2+} in gray. The positions of the R1 nitroxide labels at S17C and A128C are indicated by the red spheres located at the corresponding backbone Cα positions (for visualization purposes only). Models 1, 3, 11, and 12 are from the replica exchange solution tempering MD simulation,[33] and model 17 is the compact holo crystal structure (1PRD).[19] (B) $P(r)$ distributions calculated from the molecular coordinates[18] of the clusters (blue) compared to the $P(r)$ distribution obtained from global analysis of the DEER data at all values of T simultaneously (gray). (C) Comparison of the experimental intermolecular PRE profiles[9] (gray) with those calculated for the five models. The red circles represent the calculated PREs on the N-terminal domain arising from the R1 nitroxide spin-label attached to A128C in the C-terminal domain; the blue circles represent the calculated PREs on the C-terminal domain arising from the R1 nitroxide spin-label attached to A17C in the N-terminal domain. The interdomain PREs are normalized to the largest value. The PREs originating from the R1 nitroxide labels were calculated in Xplor-NIH[38] using a five-conformer member ensemble for the spin-label, as described previously.[9,S1]

EXPERIMENTAL SECTION

Sample Preparation. Human calmodulin (CaM) was expressed and purified in *Escherichia coli* BL21(DE3) cells, as described

https://doi.org/10.1021/jacs.2c02201
J. Am. Chem. Soc. 2022, 144, 12043−12051

previously.[9] Two site-directed mutations at A17C and A128C in the NTD and CTD domains of CaM, respectively, were introduced as sites of attachment for the nitroxide spin-labels.[9] Full deuteration was achieved by growing the bacteria in deuterated minimal medium, with U-[^{12}C/^{2}H]-glucose as the sole carbon source. R1 nitroxide labeling was carried out with *S*-(1-oxyl-2,2,5,5-tetramethyl-2,5-dihydro-1H-pyrrol-3-yl)methyl methanesulfonothioate (MTSL; Toronto Research Chemicals), as described previously.[9] The purity of A17C-R1/A128C-R1 nitroxide-labeled calmodulin was verified by mass spectrometry.

Solutions for DEER EPR comprised 50 μM CaM (A17C-R1/A128-R1), 8 mM $CaCl_2$, 100 mM NaCl, 25 mM d-HEPES pH 6.4, and 20% (v/v) d_8-glycerol, placed in 1.0 mm inner diameter (1.2 mm outer diameter) quarts EPR tubes (VitoCom). Freezing of the DEER samples was carried out using three different approaches: slow rate freezing (~40 s) by placing the EPR tube in a −80 °C freezer;[43] intermediate rate freezing (~1.5 s) by directly placing the EPR tube in liquid N_2;[43] and rapid freeze-quenching (~0.5 ms) by spraying a high-speed jet onto a spinning copper plate cooled to 77 K, as described previously.[18,45]

Q-Band DEER. Pulsed EPR data were collected at Q-band (33.8 GHz) and 50 K on a Bruker E-580 spectrometer equipped with a 150 W traveling-wave tube amplifier, a model ER5107D2 resonator, and a cryofree cooling unit, as described previously.[52] DEER experiments were acquired using a conventional four-pulse sequence (Figure S1).[53] The observer and ELDOR pump pulses were separated by ca. 90 MHz, with the observer $\pi/2$ and π pulses set to 12 and 24 ns, respectively, and the ELDOR π pulse to 10 ns. The pump frequency was centered at the Q-band nitroxide spectrum located at +40 MHz from the center of the resonator frequency. The τ_1 value of 350 ns for the first echo period time was incremented eight times in 16 ns steps to average ^{2}H modulation; the position of the ELDOR pump pulse was incremented in steps of Δt = 10 ns. The bandwidth of the overcoupled resonator was 120 MHz. All DEER echo curves were acquired for t_{max} = 7.5 μs, with the exception of the DEER echo curve for τ_2 < 7.5 μs, where t_{max} was set to the value of τ_2. DEER data were recorded with values of the dipolar evolution time T (=2τ_2) set to 10, 15, 20, 25, 30, and 35 μs. Measurement times were approximately as follows: for T = 10 μs, 3 h; 15−25 μs, 12 h; and 30−35 μs, 36 h.

Calculation of *P*(*r*) Distance Distributions from Molecular Coordinates. $P(r)$ distance distributions between pairs of R1 nitroxide spin-labels were calculated in the program Xplor-NIH[38,54] from molecular coordinates, as recently described,[18] using a rotamer library of R1 side-chain conformations whose populations consist of an intrinsic component modulated by overlap with nearby backbone atoms such that the population of a particular rotamer goes to zero when it closely approaches a backbone atom. Because the R1 nitroxide labels are represented as an ensemble, the shape of the $P(r)$ distribution can be non-Gaussian and can include shoulders and/or separate peaks that correspond to distinct regions of conformational space occupied by one or both nitroxide labels.

***P*(*r*) Distance Distributions from DEER Echo Curves.** $P(r)$ distributions from the DEER echo curves were obtained by two methods: (a) model-free validated Tikhonov regularization using the program DeerLab;[46] (b) direct fitting to the experimental DEER data (including background correction with a best-fit exponential decay) of a population-optimized sum of $P(r)$ distributions calculated from the molecular coordinates[18] of the MD clusters[33] and compact 1PRW crystal structure[19] using the fitting routines from the program DD/GLADDvu[47,48] imported into a home-written Python program.[18] Validated Tikhonov regularization was performed with bootstrap analysis for uncertainty quantification using the Bootan function in the DeerLab library, with the number of bootstrap samples evaluated set to 1000.[33] The DEER echo curves at the different values of T (ranging from 10 to 35 μs) were either fitted individually (DeerLab) or globally (DeerLab and DD/GLADDvu).

In the case of the global fits using DD/LADDvu in conjunction with the $P(r)$ distributions calculated from the coordinates of models 1−17 (see Figure 1), the calculated DEER echo curve is given by $\sum_i \varepsilon_i \{X[(P(r_i),\lambda,\Delta,t)]\}$, where ε_i is the population of model i, $X[(P(r_i),\lambda,\Delta,t)]$ is the normalized DEER echo curve for the i^{th} model, $P(r_i)$ is the probability pairwise distance distribution for model i calculated from the molecular coordinates using Xplor-NIH, λ is the exponent of the background function, Δ is the modulation depth, and t is the dipolar evolution time.[47,48] The DEER echo curves for T = 10−35 μs were fitted globally: ε_i are global parameters, while λ and Δ are local parameters specific for each value of T. $\sum_i \varepsilon_i$ is constrained to a value of 1. A two-pass iterative approach was employed for the optimization of the ε_i coefficients: initially, all ε_i were optimized; subsequently, if the optimized value of a given ε_i was found to be very small ($\leq 10^{-4}$) and ill-defined by the data, its value was set to zero, and only the ε_i coefficients of the remaining models were optimized. Calculations with various initial values of ε_i were carried out to ensure the uniqueness of the solutions: the starting ε_i values were chosen randomly within a range of ±3 to ±50% of 0.0588 (=1/17). Minimization was carried out using the Levenberg−Marquardt algorithm. The standard deviations of the ε_i values reported in Table 3 are calculated from the variance−covariance matrix.

■ ASSOCIATED CONTENT

Supporting Information

The Supporting Information is available free of charge at https://pubs.acs.org/doi/10.1021/jacs.2c02201.

Figure of the four-pulse DEER sequence used in the current work; seven figures providing the complete set of DEER echo curves and associated fits; figure showing a superposition of the $P(r)$ distributions obtained for the slow, intermediate, and fast freezing regimes; supplementary table of species populations, and χ^2 values obtained from a series of calculations in which structures within a given family with similar $P(r)$ distributions were permuted (PDF)

■ AUTHOR INFORMATION

Corresponding Author

G. Marius Clore − *Laboratory of Chemical Physics, National Institute of Diabetes and Digestive and Kidney Diseases, National Institutes of Health, Bethesda, Maryland 20892-0520, United States;* orcid.org/0000-0003-3809-1027; Email: mariusc@mail.nih.gov

Authors

Thomas Schmidt − *Laboratory of Chemical Physics, National Institute of Diabetes and Digestive and Kidney Diseases, National Institutes of Health, Bethesda, Maryland 20892-0520, United States*

David Wang − *Laboratory of Chemical Physics, National Institute of Diabetes and Digestive and Kidney Diseases, National Institutes of Health, Bethesda, Maryland 20892-0520, United States*

Jaekyun Jeon − *Laboratory of Chemical Physics, National Institute of Diabetes and Digestive and Kidney Diseases, National Institutes of Health, Bethesda, Maryland 20892-0520, United States*

Charles D. Schwieters − *Laboratory of Chemical Physics, National Institute of Diabetes and Digestive and Kidney Diseases, National Institutes of Health, Bethesda, Maryland 20892-0520, United States*

Complete contact information is available at: https://pubs.acs.org/10.1021/jacs.2c02201

https://doi.org/10.1021/jacs.2c02201
J. Am. Chem. Soc. 2022, 144, 12043−12051

Author Contributions

The manuscript was written through contributions of all authors. All authors have given approval to the final version of the manuscript.

Notes

The authors declare no competing financial interest.

■ ACKNOWLEDGMENTS

The coordinates for the molecular dynamics clusters were kindly provided to the authors by Dr. Lucie Delemotte. The authors thank Dr. Robert Best for helpful discussions and Drs. Guillermo Bejermo, Dusty Baber, Dan Garrett, and John Louis for technical support. This work was supported by the Intramural Program of the National Institute of Diabetes and Digestive and Kidney Diseases of the National Institutes of Health (to G.M.C., DK-029023).

■ REFERENCES

(1) Ramanathan, A.; Savol, A.; Burger, V.; Chennubhotla, C. S.; Agarwal, P. K. Protein Conformational Populations and Functionally Relevant Substates. *Acc. Chem. Res.* **2014**, *47*, 149−156.
(2) Eaton, W. A. Impact of Conformational Substates and Energy Landscapes on Understanding Hemoglobin Kinetics and Function. *J. Biol. Phys.* **2021**, *47*, 337−353.
(3) Frauenfelder, H.; Sligar, S. G.; Wolynes, P. G. The Energy Landscapes and Motions of Proteins. *Science* **1991**, *254*, 1598−1603.
(4) Bryngelson, J. D.; Onuchic, J. N.; Socci, N. D.; Wolynes, P. G. Funnels, Pathways, and the Energy Landscape of Protein Folding: A Synthesis. *Proteins* **1995**, *21*, 167−195.
(5) Dill, K. A. Polymer Principles and Protein Folding. *Protein Sci.* **1999**, *8*, 1166−1180.
(6) Dinner, A. R.; Sali, A.; Smith, L. J.; Dobson, C. M.; Karplus, M. Understanding Protein Folding Via Free-Energy Surfaces from Theory and Experiment. *Trends Biochem. Sci.* **2000**, *25*, 331−339.
(7) Vendruscolo, M.; Dobson, C. M. Towards Complete Descriptions of the Free-Energy Landscapes of Proteins. *Philos. Trans. R. Soc., A* **2005**, *363*, 433−450.
(8) Tang, C.; Schwieters, C. D.; Clore, G. M. Open-to-Closed Transition in Apo Maltose-Binding Protein Observed by Paramagnetic NMR. *Nature* **2007**, *449*, 1078−1082.
(9) Anthis, N. J.; Doucleff, M.; Clore, G. M. Transient, Sparsely Populated Compact States of Apo and Calcium-Loaded Calmodulin Probed by Paramagnetic Relaxation Enhancement: Interplay of Conformational Selection and Induced Fit. *J. Am. Chem. Soc.* **2011**, *133*, 18966−18974.
(10) Austin, R. H.; Beeson, K. W.; Eisenstein, L.; Frauenfelder, H.; Gunsalus, I. C. Dynamics of Ligand Binding to Myoglobin. *Biochemistry* **1975**, *14*, 5355−5373.
(11) Chin, D.; Means, A. R. Calmodulin: A Prototypical Calcium Sensor. *Trends Cell Biol.* **2000**, *10*, 322−328.
(12) Babu, Y. S.; Sack, J. S.; Greenhough, T. J.; Bugg, C. E.; Means, A. R.; Cook, W. J. Three-Dimensional Structure of Calmodulin. *Nature* **1985**, *315*, 37−40.
(13) Ikura, M.; Clore, G. M.; Gronenborn, A. M.; Zhu, G.; Klee, C. B.; Bax, A. Solution Structure of a Calmodulin-Target Peptide Complex by Multidimensional NMR. *Science* **1992**, *256*, 632−638.
(14) Meador, W. E.; Means, A. R.; Quiocho, F. A. Target Enzyme Recognition by Calmodulin: 2.4 Å Structure of a Calmodulin-Peptide Complex. *Science* **1992**, *257*, 1251−1255.
(15) Kranz, J. K.; Flynn, P. F.; Fuentes, E. J.; Wand, A. J. Dissection of the Pathway of Molecular Recognition by Calmodulin. *Biochemistry* **2002**, *41*, 2599−2608.
(16) Frederick, K. K.; Marlow, M. S.; Valentine, K. G.; Wand, A. J. Conformational Entropy in Molecular Recognition by Proteins. *Nature* **2007**, *448*, 325−329.
(17) d'Auvergne, E. J.; Griesinger, C. The Theory of Frame Ordering: Observing Motions in Calmodulin Complexes. *Q. Rev. Biophys.* **2019**, *52*, No. e3.
(18) Schmidt, T.; Jeon, J.; Yau, W. M.; Schwieters, C. D.; Tycko, R.; Clore, G. M. Time-Resolved Deer EPR and Solid-State NMR Afford Kinetic and Structural Elucidation of Substrate Binding to Ca^{2+}-Ligated Calmodulin. *Proc. Natl. Acad. Sci. U.S.A.* **2022**, *119*, No. e2122308119.
(19) Fallon, J. L.; Quiocho, F. A. A Closed Compact Structure of Native Ca^{2+}-Calmodulin. *Structure* **2003**, *11*, 1303−1307.
(20) Barbato, G.; Ikura, M.; Kay, L. E.; Pastor, R. W.; Bax, A. Backbone Dynamics of Calmodulin Studied by 15n Relaxation Using Inverse Detected Two-Dimensional NMR Spectroscopy: The Central Helix Is Flexible. *Biochemistry* **1992**, *31*, 5269−5278.
(21) Clore, G. M.; Szabo, A.; Bax, A.; Kay, L. E.; Driscoll, P. C.; Gronenborn, A. M. Deviations from the Simple Two Parameter Model Free Approach to the Interpretation of ^{15}N Nuclear Magnetic Relaxation of Proteins. *J. Am. Chem. Soc.* **1990**, *112*, 4989−4991.
(22) Baber, J. L.; Szabo, A.; Tjandra, N. Analysis of Slow Interdomain Motion of Macromolecules Using NMR Relaxation Data. *J. Am. Chem. Soc.* **2001**, *123*, 3953−3959.
(23) Bertini, I.; Del Bianco, C.; Gelis, I.; Katsaros, N.; Luchinat, C.; Parigi, G.; Peana, M.; Provenzani, A.; Zoroddu, M. A. Experimentally Exploring the Conformational Space Sampled by Domain Reorientation in Calmodulin. *Proc. Natl. Acad. Sci. U.S.A.* **2004**, *101*, 6841−6846.
(24) Bertini, I.; Gupta, Y. K.; Luchinat, C.; Parigi, G.; Peana, M.; Sgheri, L.; Yuan, J. Paramagnetism-Based NMR Restraints Provide Maximum Allowed Probabilities for the Different Conformations of Partially Independent Protein Domains. *J. Am. Chem. Soc.* **2007**, *129*, 12786−12794.
(25) Bertini, I.; Giachetti, A.; Luchinat, C.; Parigi, G.; Petoukhov, M. V.; Pierattelli, R.; Ravera, E.; Svergun, D. I. Conformational Space of Flexible Biological Macromolecules from Average Data. *J. Am. Chem. Soc.* **2010**, *132*, 13553−13558.
(26) Dasgupta, S.; Hu, X.; Keizers, P. H.; Liu, W. M.; Luchinat, C.; Nagulapalli, M.; Overhand, M.; Parigi, G.; Sgheri, L.; Ubbink, M. Narrowing the Conformational Space Sampled by Two-Domain Proteins with Paramagnetic Probes in Both Domains. *J. Biomol. NMR* **2011**, *51*, 253−263.
(27) Gigli, L.; Andralojc, W.; Dalaloyan, A.; Parigi, G.; Ravera, E.; Goldfarb, D.; Luchinat, C. Assessing Protein Conformational Landscapes: Integration of DEER Data in Maximum Occurrence Analysis. *Phys. Chem. Chem. Phys.* **2018**, *20*, 27429−27438.
(28) Andrałojć, W.; Luchinat, C.; Parigi, G.; Ravera, E. Exploring Regions of Conformational Space Occupied by Two-Domain Proteins. *J. Phys. Chem. B* **2014**, *118*, 10576−10587.
(29) Anthis, N. J.; Clore, G. M. The Length of the Calmodulin Linker Determines the Extent of Transient Interdomain Association and Target Affinity. *J. Am. Chem. Soc.* **2013**, *135*, 9648−9651.
(30) Clore, G. M.; Bax, A.; Ikura, M.; Gronenborn, A. M. Structure of Calmodulin-Peptide Complexes. *Curr. Opin. Struct. Biol.* **1993**, *134*, 14686−14689.
(31) Johnson, C. K. Calmodulin, Conformational States, and Calcium Signaling. A Single-Molecule Perspective. *Biochemistry* **2006**, *45*, 14233−14246.
(32) Wyttenbach, T.; Grabenauer, M.; Thalassinos, K.; Scrivens, J. H.; Bowers, M. T. The Effect of Calcium Ions and Peptide Ligands on the Relative Stabilities of the Calmodulin Dumbbell and Compact Structures. *J. Phys. Chem. B* **2010**, *114*, 437−447.
(33) Westerlund, A. M.; Delemotte, L. Inflecs: Clustering Free Energy Landscapes with Gaussian Mixtures. *J.Chem. Theory Comput.* **2019**, *15*, 6752−6759.
(34) Westerlund, A. M.; Delemotte, L. Effect of Ca^{2+} on the Promiscuous Target-Protein Binding of Calmodulin. *PLoS Comput. Biol.* **2018**, *14*, No. e1006072.
(35) Jeschke, G. Deer Distance Measurements on Proteins. *Annu. Rev. Phys. Chem.* **2012**, *63*, 419−446.

https://doi.org/10.1021/jacs.2c02201
J. Am. Chem. Soc. 2022, 144, 12043−12051

(36) Todd, A. P.; Cong, J.; Levinthal, F.; Levinthal, C.; Hubbell, W. L. Site-Directed Mutagenesis of Colicin E1 Provides Specific Attachment Sites for Spin Labels Whose Spectra Are Sensitive to Local Conformation. *Proteins* **1989**, *6*, 294−305.
(37) Hubbell, W. L.; Cafiso, D. S.; Altenbach, C. Identifying Conformational Changes with Site-Directed Spin Labeling. *Nat. Struct. Biol.* **2000**, *7*, 735−739.
(38) Schwieters, C. D.; Bermejo, G. A.; Clore, G. M. Xplor-NIH for Molecular Structure Determination from Nmr and Other Data Sources. *Protein Sci.* **2018**, *27*, 26−40.
(39) Ward, R.; Bowman, A.; Sozudogru, E.; El-Mkami, H.; Owen-Hughes, T.; Norman, D. G. Epr Distance Measurements in Deuterated Proteins. *J. Magn. Reson.* **2010**, *207*, 164−167.
(40) Baber, J. L.; Louis, J. M.; Clore, G. M. Dependence of Distance Distributions Derived from Double Electron-Electron Resonance Pulsed EPR Spectroscopy on Pulse-Sequence Time. *Angew. Chem., Int. Ed.* **2015**, *54*, 5336−5339.
(41) Schmidt, T.; Walti, M. A.; Baber, J. L.; Hustedt, E. J.; Clore, G. M. Long Distance Measurements up to 160 a in the Groel Tetradecamer Using Q-Band DEER EPR Spectroscopy. *Angew. Chem., Int. Ed.* **2016**, *55*, 15905−15909.
(42) Schmidt, T.; Clore, G. M. T_m Filtering by ^{1}H-Methyl Labeling in a Deuterated Protein for Pulsed Double Electron-Electron Resonance EPR. *Chem. Commun.* **2020**, *56*, 10890−10893.
(43) Georgieva, E. R.; Roy, A. S.; Grigoryants, V. M.; Borbat, P. P.; Earle, K. A.; Scholes, C. P.; Freed, J. H. Effect of Freezing Conditions on Distances and Their Distributions Derived from Double Electron Electron Resonance (DEER): A Study of Doubly-Spin-Labeled T4 Lysozyme. *J. Magn. Reson.* **2012**, *216*, 69−77.
(44) Jeon, J.; Thurber, K. R.; Ghirlando, R.; Yau, W. M.; Tycko, R. Application of Millisecond Time-Resolved Solid State NMR to the Kinetics and Mechanism of Melittin Self-Assembly. *Proc. Natl. Acad. Sci. U.S.A.* **2019**, *116*, 16717−16722.
(45) Schmidt, T.; Jeon, J.; Okuno, Y.; Chiliveri, S. C.; Clore, G. M. Submillisecond Freezing Permits Cryoprotectant-Free EPR Double Electron-Electron Resonance Spectroscopy. *ChemPhysChem* **2020**, *21*, 1224−1229.
(46) Fábregas Ibáñez, L.; Jeschke, G.; Stoll, S. Deerlab: A Comprehensive Software Package for Analyzing Dipolar Electron Paramagnetic Resonance Spectroscopy Data. *Magn. Reson.* **2020**, *1*, 209−224.
(47) Brandon, S.; Beth, A. H.; Hustedt, E. J. The Global Analysis of DEER Data. *J. Magn. Reson.* **2012**, *218*, 93−104.
(48) Hustedt, E. J.; Stein, R. A.; McHaourab, H. S. Protein Functional Dynamics from the Rigorous Global Analysis of DEER Data: Conditions, Components, and Conformations. *J. Gen. Physiol.* **2021**, *153*, No. e201711954.
(49) Westerlund, A. M.; Harpole, T. J.; Blau, C.; Delemotte, L. Inference of Calmodulin's Ca^{2+}-Dependent Free Energy Landscapes Via Gaussian Mixture Model Validation. *J. Chem. Theory Comput.* **2018**, *14*, 63−71.
(50) Clore, G. M.; Iwahara, J. Theory, Practice, and Applications of Paramagnetic Relaxation Enhancement for the Characterization of Transient Low-Population States of Biological Macromolecules and Their Complexes. *Chem. Rev.* **2009**, *109*, 4108−4139.
(51) Iwahara, J.; Schwieters, C. D.; Clore, G. M. Ensemble Approach for Nmr Structure Refinement against ^{1}H Paramagnetic Relaxation Enhancement Data Arising from a Flexible Paramagnetic Group Attached to a Macromolecule. *J. Am. Chem. Soc.* **2004**, *126*, 5879−5896.
(52) Schmidt, T.; Schwieters, C. D.; Clore, G. M. Spatial Domain Organization in the HIV-1 Reverse Transcriptase P66 Homodimer Precursor Probed by Double Electron-Electron Resonance EPR. *Proc. Natl. Acad. Sci. U.S.A.* **2019**, *116*, 17809−17816.
(53) Pannier, M.; Veit, S.; Godt, A.; Jeschke, G.; Spiess, H. W. Dead-Time Free Measurement of Dipole-Dipole Interactions between Electron Spins. *J. Magn. Reson.* **2000**, *142*, 331−340.
(54) Schwieters, C. D.; Kuszewski, J. J.; Tjandra, N.; Clore, G. M. The Xplor-NIH NMR Molecular Structure Determination Package. *J. Magn. Reson.* **2003**, *160*, 65−73.

https://doi.org/10.1021/jacs.2c02201
J. Am. Chem. Soc. 2022, 144, 12043−12051